Universiteit Utrecht

Bachelor thesis

The Origin of Hoag's Object

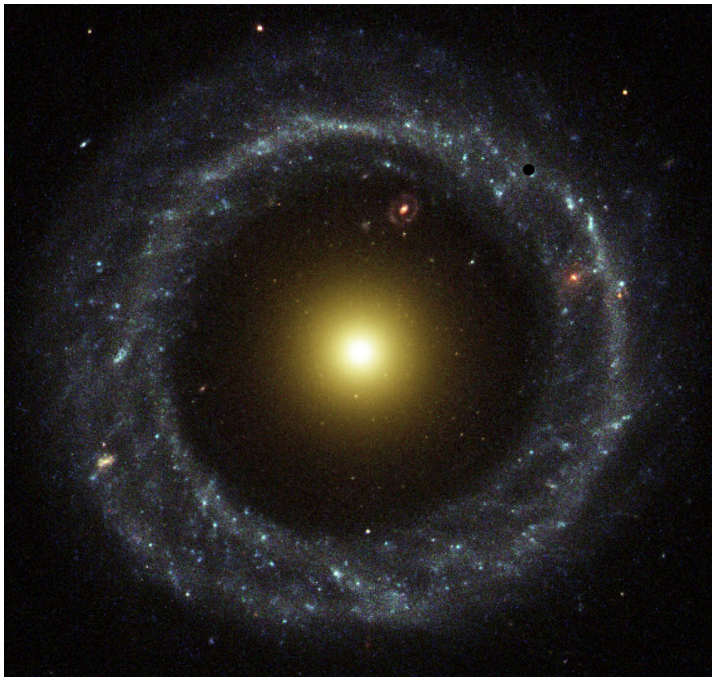

Author:
Lars van den Haak
Study: Physics & Mathematics

Supervisors:
Simon Portegies Zwart
Leiden University
and
Jeroen Bédorf
Leiden University
and
Gerard Barkema
Utrecht University

June 15, 2016

The Origin of the Hoag's Object

Lars van den Haak[1] and Jeroen Bédorf, Simon Portegies Zwart[2]
[1] *Utrecht University*
[2] *Leiden University*

(Dated: June 15, 2016)

In this research we look if we can recreate Hoag's Object from standard galaxy models without other interactions. We run our simulations with 16 million particles for 97.7 Gyr, more than six times the Hubble time. Our initial model has three parts, a Sérsic bulge, an exponential disk and a NFW halo. We used the Bonsai code, a tree code that uses the Graphics Processing Unit (GPU). We conclude that we did not succeed in recreating Hoag's Object. A ring forms, but there is also a strong bar present. The bar strength initially grows and stays equal after 50 Gyr. The bar speed slows down exponentially. The galaxy reaches an equilibrium after 50 Gyr. We propose some initial parameters that could help destroy the bar, with the mention of a Central Mass Density.

I. INTRODUCTION

Hoag's Object is a remarkable object, first observed by Arthur Hoag (1950). It is quite a peculiar object, around the central bulge of stars it has an almost perfect circular ring with stars. There have been several studies (Brosch (1985), Schweizer *et al.* (1987), Freeman, Howard, and Byrd (2010), Finkelman *et al.* (2011), Brosch *et al.* (2013)) about the origin of this object and we will explore one hypothesis of it in this article.

Our interest in Hoag's Object origins from a simulation of the Milky Way in 2014 by Bédorf *et al.* (2014). The simulations ran longer than intended and after a week there seemed to emerge a Hoag type galaxy. The simulation time was more than the Hubble time, but this still piqued our curiosity. This study tries to reproduce these results and look if there are initial conditions such that a ring like structure could come into existence in less than the Hubble time. Fig. 1 shows a picture of Hoag's Object, taken by the Hubble Space Telescope.

The following section contains a theoretical background we need to analyze and understand our results. The third section contains the properties of Hoag's Object obtained from observations of previous studies. In the fourth section we will point out the different hypothesis about the origin and end with hypotheses we research in this article. In the fifth section we describe the details of our simulations. In the sixth section we present our result and in the last two section we discuss the results and give our conclusions.

II. THEORY

In this section we will discuss the theoretical background needed to understand the rest of this thesis. We discuss some basic terms and the Lindblad Resonance.

A. Basic Terms

Here I introduce most terms that are used in this work. We divide spiral galaxies in three parts: the bulge, the disk and the halo. The bulge is the inner part of a galaxy, here the density of stars

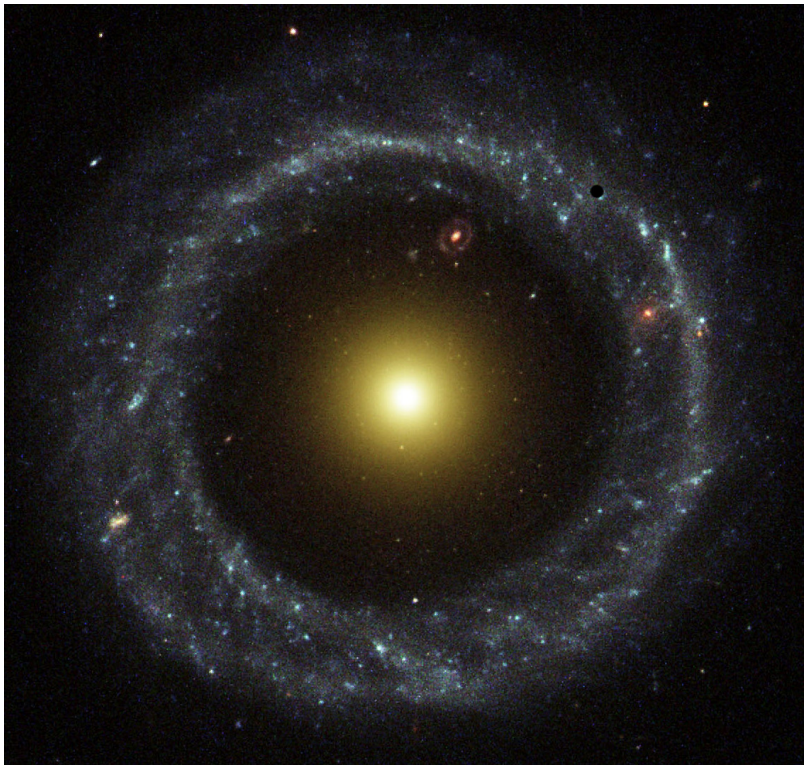

FIG. 1 Hoag's Object as seen by the Hubble Space Telescope. (Image credit: R. Lucas (STScI/AURA), Hubble Heritage Team, NASA)

is higher. It is found in most spiral galaxies. The disk is the other visible part of the galaxy, here the stars orbit the center of a galaxy in a thin disk. Lastly we have the halo, this consist mostly of dark matter. This is matter that we, as of yet, cannot see or observe except for their gravitational force on the stars. Spiral galaxies are called this way, because you can see spirals in them if we look at them from above. A special case of a spiral is a bar, as is best described by a picture, see Fig. 2. Here you also see the spiral arms starting at the tips of the bar.

Astronomy uses a different set of units for some physical quantities. We will explain them here. Parsec (pc) is a unit of length, one unit equals 3.086×10^{16} metres. Arcsec ($''$) is a unit of angular measurement, it is equal to $\frac{1}{3600}$ of a degree. or $\frac{\pi}{648000}$ radians. The solar mass ($M_\odot$) is a mass unit, one unit equals 1.989×10^{30} kg. It is also equal to the mass of the sun. Solar luminosity ($L_\odot$) is a unit of luminosity, one unit equals $3.846 \times 10^{26} W$. It is also equal to the luminosity of the sun. Luminosity (L) is the total amount of energy emitted by an object per unit time. Flux (F) is the luminosity per area. The relation between flux and luminosity is $L = 4\pi d^2 F$, where d is the distance between the observer and the object. Apparent magnitude (m) is a measure of brightness as seen by an observer on Earth. The relation between apparent magnitude in spectral band x and flux is defined by $m_x = -2.5 \log_{10}(\frac{F_x}{F_{x,0}})$ Where F_x is the observed flux with spectral filter x and $F_{x,0}$ is a reverence flux. Spectral filters are used to measure flux at certain wavelengths. Commonly

FIG. 2 Barred Spiral Galaxy NGC 1300 as seen by the Hubble Space Telescope. (Image credit: NASA, ESA, and The Hubble Heritage Team STScI/AURA)

used are U (ultraviolet) at an effective wavelength of 365 nm, B (blue) at 445 nm, V (visual) at 551 nm, R (red) for 658 nm and I (infrared) at 806 nm.

B. Lindblad resonances

The following section is based on section 3.3 from Binney and Tremaine (2008). Linblad resonance occurs in galaxies with a non-axisymmetric potential. In other words galaxies with spirals or bars. We assume a galaxy with a weak bar. The bar rotates with a pattern speed which we will call Ω_b. We look at the orbit of a star in this galaxy. We only look at it from the top, so we discard the z-coordinate which makes it a 2D system. We use polar coordinates (R, φ) for the frame that rotates with the same pattern speed as the bar. We let $\varphi = 0$ be in the direction of the bar. This gives us the following Lagrangian per unit mass

$$\mathcal{L} = \frac{1}{2}\dot{R} + \frac{1}{2}[R(\dot{\varphi} + \Omega_b)]^2 - \Phi(R, \varphi). \tag{2.1}$$

Where $\Phi(R, \varphi)$ is the potential. The resulting equations of motion are

$$\ddot{R} = R(\dot{\varphi} + \Omega_b)^2 - \frac{\partial \Phi}{\partial R}, \tag{2.2a}$$

$$\frac{d}{dt}[R^2(\dot{\varphi} + \Omega_b)] = -\frac{\partial \Phi}{\partial \varphi}. \tag{2.2b}$$

We assume a weak bar, therefore we divide the potential in a part that is axisymmetric and in a part that is not.

$$\Phi(R, \varphi) = \Phi_0(R) + \Phi_1(R, \varphi) \tag{2.3}$$

where $|\frac{\Phi_1(R,\varphi)}{\Phi_0(R)}| \ll 1$. Next we divide R and φ in zeroth- and first-order parts

$$\begin{aligned} R(t) &= R_0 + R_1(t), \\ \varphi(t) &= \varphi_0(t) + \varphi_1(t). \end{aligned} \tag{2.4}$$

We fill in these above expressions in equation 2.2 and require that the zeroth-order terms sum to zero.

$$\begin{aligned} R_0(\dot{\varphi}+\Omega_b)^2 &= \left(\frac{d\Phi_0}{dR}\right)_{R_0}, \\ \dot{\varphi}_0 &= \text{constant}. \end{aligned} \tag{2.5}$$

Essentially it says that the force on a particle is the same as the centrifugal force. So the motion induced by the zero-order terms is a perfect circle with radius R_0. We define $\Omega(R)$ as the circular frequency in potential Φ_0, defined by

$$\Omega(R) \equiv \pm\sqrt{\frac{1}{R}\frac{d\Phi_0}{dR}}. \tag{2.6}$$

Further more we define $\Omega_0 \equiv \Omega(R_0)$. With this equation 2.5 becomes

$$\dot{\varphi}_0 = \Omega_0 - \Omega_b. \tag{2.7}$$

Where $\Omega_0 > 0$ for orbits that move in the same direction as the bar and $\Omega_0 < 0$ moves in the other direction. Thus setting $\varphi_0(0) = 0$ gives us

$$\varphi_0(t) = (\Omega_0 - \Omega_b)t. \tag{2.8}$$

The first order terms of equation 2.2 then become

$$\ddot{R}_1 + (\frac{d^2\Phi_0}{dR^2} - \Omega^2)_{R_0}R_1 - 2R_0\Omega_0\dot{\varphi}_1 = -(\frac{\partial\Phi_1}{\partial R})_{R_0}, \tag{2.9a}$$

$$\ddot{\varphi}_1 + 2\Omega_0\frac{\dot{R}_1}{R_0} = -\frac{1}{R_0^2}(\frac{\partial\Phi_1}{\partial\varphi})_{R_0}. \tag{2.9b}$$

To go any further, we must specify the form of ϕ_1 some more. We use

$$\Phi_1(R,\varphi) = \Phi_b(R)\cos(m\varphi) \tag{2.10}$$

Here m is a positive integer. It means that our potential has a spiral symmetry. In case of a bar we set $m = 2$. Since we require that the bar is aligned along $\varphi = 0$, the potential over there is at it's lowest, since most of it's mass is there. Therefor we require that $\Phi_b < 0$. We assume that the angular velocity $\dot{\varphi}_1$ is small and that φ_1 is small, thus the perturbation in φ is small. With this $\varphi_1 \ll 1$, so $\varphi(t)$ stays close to $(\Omega_0 - \Omega_b)t$. Now we can replace φ by φ_0 in our first-order equations 2.9

$$\ddot{R}_1 + (\frac{d^2\Phi_0}{dR^2} - \Omega^2)_{R_0}R_1 - 2R_0\Omega_0\dot{\varphi}_1 = -(\frac{d\Phi_b}{dR})_{R_0}\cos[m(\Omega_0 - \Omega_b)t], \tag{2.11a}$$

$$\ddot{\varphi}_1 + 2\Omega_0\frac{\dot{R}_1}{R_0} = -\frac{m\Phi_b(R_0)}{R_0^2}\sin[m(\Omega_0 - \Omega_b)t]. \tag{2.11b}$$

We integrate the latter of these equations to obtain

$$\dot{\varphi}_1 = -2\Omega_0 \frac{R_1}{R_0} - \frac{\Phi_b(R_0)}{R_0^2(\Omega_0 - \Omega_b)} \cos[m(\Omega_0 - \Omega_b)t] + constant. \tag{2.12}$$

We use this in equation 2.11a and we get

$$\ddot{R}_1 + \kappa_0^2 R_1 = -[\frac{d\Phi_b}{dR} + \frac{2\Omega\Phi_b}{R(\Omega - \Omega_b)}]_{R_0} \cos[m(\Omega_0 - \Omega_b)t] + constant, \tag{2.13a}$$

where

$$\kappa_0^2 \equiv (\frac{d^2\Phi_0}{dR^2} + 3\Omega^2)_{R_0} = (R\frac{d\Omega^2}{dR} + 4\Omega^2)_{R_0}. \tag{2.13b}$$

Here κ_0 is what we call the epicycle frequency. The constant in the above equation isn't really important, since we can shift it with $R_1 \to R_1 + constant$. If we look at equation 2.13a we see that this is a differential equation for the driven harmonic oscillator. It has natural frequency κ_0 and a driven frequency of $m(\Omega_0 + \Omega_b)$. The general solution to this equation is

$$R_1(t) = C_1 \cos(\kappa_o t + \alpha) - [\frac{d\Phi_b}{dR} + \frac{2\Omega\Phi_b}{R(\Omega - \Omega_b)}]_{R_0} \frac{\cos[m(\Omega_0 - \Omega_b)t]}{\Delta} \tag{2.14a}$$

where C_1 and α are constants and

$$\Delta \equiv \kappa_0^2 - m^2(\Omega_0 - \Omega_b)^2. \tag{2.14b}$$

We can now use equation 2.8 to get out the time. We get

$$R_1(\varphi_0) = C_1 \cos(\frac{\kappa_0\varphi_0}{\Omega_0 - \Omega_b} + \alpha) + C_2 \cos(m\varphi_0) \tag{2.15a}$$

where

$$C_2 \equiv -\frac{1}{\Delta}[\frac{d\Phi_b}{dR} + \frac{2\Omega\Phi_b}{R(\Omega - \Omega_b)}]_{R_0}. \tag{2.15b}$$

If we set $C_1 = 0$ we only get the second cos which has period $\frac{2\pi}{m}$. This is a closed loop orbit, an orbit that closes on itself again after a number of rotations and thus repeats itself. The orbits with $C_1 \neq 0$ are non-closed loop orbits.

There are a few values for which equation 2.15a becomes singular. These are the resonances. The corotation resonance happens when

$$\Omega_0 = \Omega_b. \tag{2.16}$$

This implies that $\dot{\varphi}_0 = 0$. In this case the φ_0 co-rotates with the same speed as the potential. For $m = 2$ this is the same speed as the bar.

The Linblad resonances happens at

$$m(\Omega_0 - \Omega_b) = \pm\kappa_0. \tag{2.17}$$

In this case the star comes across the crests of the potential at the same frequency of its epicycle frequency κ_0.

Near these Linblad resonances, Δ becomes small, so C_2 becomes large. Therefor particles there have a large radial force acting on them, this could lead to shocks and thus to rapid star formation. These regions might then become visible as rings (Buta, 1995).

III. PROPERTIES OF HOAG'S OBJECT

In this section we present the properties of Hoag's Object that are obtained from observational data generated by previous studies. This will be important for making an initial model and to compare our simulation results against. Unless stated otherwise the data is obtained from Finkelman *et al.* (2011).

Hoag's Object is found at a right ascension of $15^h17^m14.405^s$ and a declination of $+21°35'07.88''$ in the J2000 coordinate system (obtained from NED, NASA/IPAC Extragalactic Database). The receding velocity is $V_{sys} = 12767 \pm 3$km s^{-1} for the core and $V_{sys} = 12761 \pm 4$km s^{-1} for the ring.

We assume the Hubble constant $H_0 = 73$km s^{-1}, $\Omega_m = 0.27$ and $\Omega_\Lambda = 0.73$. Ω_m and Ω_Λ are mass and energy density parameters respectively of the whole Universe. With this the calculated distance of Hoag's Object is 175.5 Mpc and the scale is 851pc arcsec^{-1}.

A. Luminosity

The observational data of the core was fitted to an exponential disk and Sérsic Bulge[1]. It gives a Sérsic index of $n = 3.9 \pm 0.2$, an effective radius of $r_e = 2.8 \pm 0.1$ arcsec $= 2.5 \pm 0.1$ kpc and an effective surface magnitude of $\mu_B \sim 22.6 \pm 0.5$ mag arcsec^{-2}. The total luminosity of the core is $\mu_B = 16.98 \pm 0.01$ mag in blue light and $\mu_I = 14.47 \pm 0.01$ mag in infrared light.

Fig. 3 shows the azimuthally averaged luminosity profile of Hoag's Object at each radius. The profile follows a power-law up to ~ 11 arcsec $= 9$ kpc, it has a sharp transition at ~ 13 arcsec $= 11$ kpc, which corresponds with the inner edge of the ring. The outer edge is lies at ~ 27 arcsec $= 23$ kpc. It has a flat luminosity profile between 17 and 22 arcsec (14-19 kpc).

B. Kinematics

Within $r < r_e$ the calculated effective velocity dispersion is $\sigma = 151 \pm 5$km s^{-1}, which is consistent with Schweizer *et al.* (1987). The ring and core are slightly inclined to the sky with an angle of $19° \pm 5°$ for the core and $18° \pm 4°$ for the ring. This can be seen in Fig. 2 of Finkelman *et al.* (2011). The primary axis of this inclination has a position angle[2] (PA) of $41° \pm 5°$ for the core and

---

[1] A Sérsic profile is function that describes how the intensity I of galaxy relates to the distance R from its center. It has the form $I(R) \propto e^{-kR^{1/n}}$ and n is the Sérsic index.

[2] The position angle is defined as the angle measured counterclockwise relative to the north celestial pole

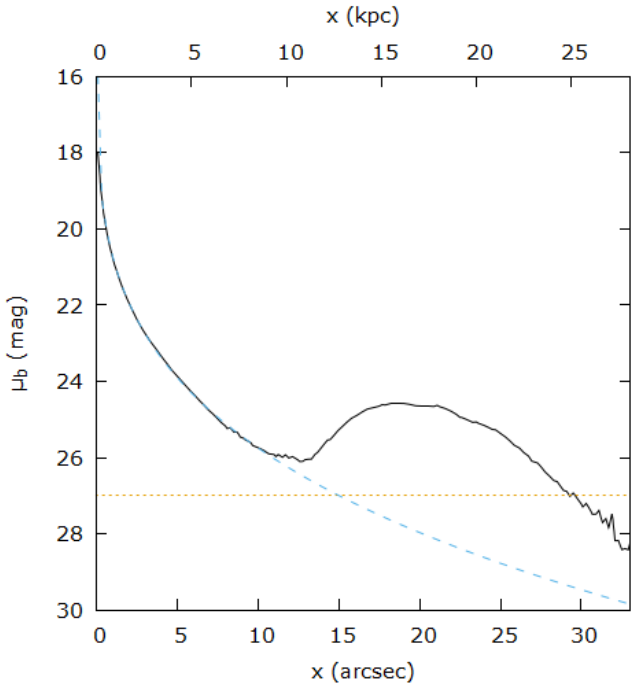

FIG. 3 Azimuthally averaged luminosity profile of Hoag's Object. The dashed horizontal line represents the background noise. The other dashed line represent the power-law fit up to 11 arcsec. This figure is obtained from Finkelman *et al.* (2011).

$43° \pm 3°$ for the ring. The maximum rotational velocity that is measured for the core is 70km s^{-1} at 4 arcsec = 3.4 kpc. This is lower than the real value, since it isn't seen straight on. A fitted model to the data gave a maximum rotational velocity of 180km s^{-1} at 6 arcsec = 5.1 kpc for the core.

With a model for the ring a rotational speed of about 260 km s^{-1} across the whole ring is obtained, see the tilted ring method in fig. 11 in Finkelman *et al.* (2011).

C. Star population

There are two analyses made of Hoag's Object central core. One shows that the core formed more then 9 Gyr's ago, but a small fraction is ~ 0.5 Gyr stars. The other shows that the central core population is well matched by a single $\gtrsim 10$ Gyr old stellar population.

The fit for the ring is in agreement with a ~ 2 Gyr stellar population, although there are signs for ongoing star formation.

Object/Parameter	HO	O1	O2	G1
α J2000	$15^h17^m14^s$	$15^h17^m40^s$	$15^h16^m09^s$	$15^h16^m01^s$
δ J2000	$+21°35'08''$	$+21°36'19''$	$+21°36'10''$	$+21°32'27''$
cz. (km s^{-1})	12736	12700	12629	12676
M(HI) (10^9M.)	6.2	0.39	1.2	

TABLE I Objects near Hoag's Object. First two rows are the position in the J2000 coordinate system. The next row is the receding velocity measured by the redshift. The last row is the mass of the HI content, if present. This table is the obtained from Brosch *et al.* (2013)

D. Environment

Brosch *et al.* (2013) has done a study of the H1 content in Hoag's Object and other objects near this galaxy. The mass of the HI cloud is $M(HI) = 6.2 \times 10^9 M.$ with an uncertainty of 10 percent. The HI ring is best fitted by two separate rings. The first having a radius between 14 and 28 arcsec (16 and 33 kpc) and inclined to the sky with an angle of $\sim 18°$. The second one has a radius between 28 and 42 arcsec (33 and 49 kpc) and is inclined to the sky with an angle of $\sim 25°$. There are three objects found near Hoag's Object, two H1 clouds and one galaxy. They are summarized in table I.

E. Lindblad Resonance

In case the morphology of Hoag's Object was created by a bar (see section IV.E), we would expect the outer ring to coincide with the outer Lindblad resonance. We will follow the work of Byrd, Freeman, and Buta (2006) and Freeman, Howard, and Byrd (2010). First we need a model to calculate the radii for the resonance. We use a simple axisymteric potential for the zero-order term of the potential

$$\Phi_0 = \frac{1}{2} v_0^2 \ln(R_c + R), \tag{3.1}$$

where R_c is the core radius, defining the potential for small R, v_c is a constant that determines the rotational speed. With equation 2.6 we get the circular frequency

$$\Omega(R) = \frac{v_0}{\sqrt{R_c^2 + R^2}} \rightarrow \frac{v_0}{R} \text{ for } R \gg R_c. \tag{3.2}$$

With this we can calculate the epicycle frequency κ (see equation 2.13b)

$$\kappa^2 = 2\frac{v_0^2}{R^2}. \tag{3.3}$$

The Lindblad resonance we have derived in equation 2.17 must hold for $m = 2$. In this case we get

$$2(\frac{v_0}{R} - \Omega_b) = \pm\sqrt{2}\frac{v_0}{R}, \tag{3.4}$$

where Ω_b was the bar (pattern) speed. For the co-rotation radius (R_{CR}) $\Omega_b = \frac{v_0}{R_{CR}}$ must hold. With this we solve the above equation and get

$$R_{ILR} = (1 - \frac{1}{2}\sqrt{2})R_{CR}, \tag{3.5a}$$

$$R_{OLR} = (1 + \frac{1}{2}\sqrt{2})R_{CR}, \tag{3.5b}$$

where R_{ILR} and R_{OLR} are the radius for the inner and outer Lindblad resonance. With a rotational speed of 260km s^{-1} observed in the ring, we choose this as constant across our model. With this and expecting to see the ring at the outer Lindblad resonance, we can scale the other radii. The ring begins at 15.5 arcsec = 13.2 kpc, thus R_{OLR} = 13.2 kpc, R_{CR} = 7.7 kpc and R_{ILR} = 2.3 kpc. Note that the inner Lindblad resonance comes quite close to $r_e = 2.5 \pm 0.1$ kpc for the core of Hoag's Object. The bar speed is then $\Omega_b = \frac{260}{7.7} = 33.6$ km s^{-1} kpc^{-1}.

It must be noted that this is a very crude approximation of Hoag's Object. For one, we have seen that the observed rotational speed is not constant across the whole galaxy. It gives an idea of the order of the bar speed.

IV. HYPOTHESES OF THE ORIGIN OF THE HOAG'S OBJECT

A. Gravitational lens

For this hypothesis we need a massive object between us and a source of light. This massive object bends the light of the source with its gravity in such a way that we see the source as the ring of Hoags Object. The massive object itself acts as the core. This hypothesis was put forward by Hoag (1950) himself, but stated that it was a not so likely explanation. If it is true, the core should be extremely massive. However observations from Schweizer *et al.* (1987) show us that the ring and bulge have the same redshift, hence are at the same distance and physically belong to the same system. This is not the case for gravitational lenses, therefore this hypothesis can be discarded.

B. Collision between galaxies

An other possible explanation is a head-on collision with two galaxies. This mechanism is similar to the famous Cartwheel Galaxy (Amram *et al.*, 1998). A smaller galaxy collides with a bigger, where the smaller one acts like a bullet. It sweeps out the stars in the center and the ring is the only thing that remains of the bigger galaxy. If Hoag's Object is formed like this, the collision must be seen head-on. Schweizer *et al.* (1987) argued that the radial velocity difference between the ring and core should be of the order of 10^2 km s^{-1} for a collision. But we observe a velocity difference of only 6 ± 5 km s^{-1}.

We mentioned in section III.D that there are three objects near Hoag's Object. Two H1 clouds at $\sim$ 300 kpc and $\sim$ 1 Mpc. The closest one has no visible optical counterpart. If we suppose there once was an optical counterpart, it could have disappeared by an interaction with Hoag's Object. This interaction must have occurred more then $1 \sim 2$ Gyr ago if we assume a relative velocity of 200 km s^{-1}. But if it acted like a bullet, we would expect to see it somewhere else on the sky. So we see no other galaxy that could have acted like a bullet.

These two arguments make this hypothesis unlikely.

C. Major Accretion event

A major accretion event is a collision (not head-on) or close encounter of two galaxies. Schweizer *et al.* (1987) put this hypothesis forward. One galaxy transfers some or all of it's mass to the other one. For the Hoag's Object we suppose that the central core was one galaxy and the ring is the mass transfer of the other galaxy.

We will now follow the discussion of Finkelman *et al.* (2011). Schweizer *et al.* (1987) argues that the event must have taken place $2 \sim 3$ Gyr ago. If it was more recent, we would see evidence in form of a tidal tail or ripple signatures. As we mentioned, the ring has a stellar population of ~ 2 Gyr and the gas needs at least ~ 1 Gyr to settle in a circular orbit. This is consistent with the hypothesis.

But with the total measured blue light coming from the ring, the mass of the ring must be at least $3 \times 10^9 M_\odot$. An estimation of the star formation rate is $\sim 0.7 M_\odot yr^{-1}$. This star formation rate would have formed the ring in more than 4 Gyr.

Furthermore the initial mass of the HI gas in the disk should be over $10^{10} M_\odot$, if we look at the mass of the HI cloud and the ring now. This is twice that of the Milky Way and at least an order of magnitude larger than dwarf irregular galaxies contain. This implies that the mass couldn't be transferred in just one accretion event from a dwarf galaxy. A merger of two equal-mass galaxies could be possible. In that case some of the initial gas should fall into the core and cause star formation. From section III.C we have two analyses of the star population of Hoag's Object core. One shows that the core formed more then 9 Gyr's ago, but a small fraction is ~ 0.5 Gyr stars. The other matches it with a $\gtrsim 10$ Gyr stellar population. The first one is in agreement with this hypothesis.

The kinematics don't support this hypothesis. Most numerical simulations of mergers produce galaxies that are more elliptic and also produce bars.

D. Cold Accretion

This hypothesis was put forward by Finkelman *et al.* (2011). The idea is that the core is formed from a collapse of the HI cloud. After this collapse there is continuous accretion of gas from the Inter Galactic Medium (IGM). Due to the low gas density outside the core, there is no star formation. In section III.B we mention that Hoag's Object is inclined to the sky, meaning that it has a elongated triaxial core. This produces a non-axisymmetric potential which gives rise to resonances, also discussed in section II.B. These resonances compress the gas, which would bring it just above a density such that star formation takes place. This would give the gap between the ring and core of Hoag's Object.

E. Bar Instability

The original idea of a bar instability was brought forward by Brosch (1985). For Hoag's Object we assume a typical disk, in which a bar has formed. Due to this bar, there are several resonances where more mass will accumulate. One such resonance is then responsible for the ring of Hoag's Object. Because of the fact that we don't see a bar, there must have been a bar instability such that the bar disappeared. Schweizer *et al.* (1987) observed a far larger HI cloud than Brosch (1985). A large HI cloud would stabilize the galaxy against a bar instability. Furthermore, the shape and

Halo				Bulge		
a_h (kpc)	σ_h (km s^{-1})	$1-\epsilon_h$	α_h	a_b (kpc)	σ_b (km s^{-1})	$1-\epsilon_b$
9.0	290	0.95	0.5	0.64	300	0.85
Disk						
M_d ($10^{10} M_\odot$)	R_d (kpc)	z_d (kpc)	σ_{R0} (km s^{-1})	R_{out} (kpc)	δR_{out} (kpc)	
4.9	4.2	0.36	74.2	45	0.8	

TABLE II The parameters we use in our simulation model. For the Halo we have the scale radius (a_h), the characteristic velocity dispersion (σ_h), the truncation parameter (ϵ_h) and the rotation parameter (α_h). For the Bulge we have the scale length (a_b), the characteristic velocity (σ_b) and the truncation parameter (ϵ_b). The last being the the disk, here we have the disk Mass (M_d), the disk scale length (R_d), the disk scale height (z_d), the radial velocity dispersion at the center (σ_{R0}), the cut-off radius R_{out} and the radial range for disk truncation δR_{out}.

dynamics of the core give evidence for an elliptic shaped galaxy, where we do not expect bars. Also the age between the stars in the ring and core would be more alike, since it came from the same population. Thus both Schweizer *et al.* (1987) and Finkelman *et al.* (2011) deem this an unlikely scenario.

Freeman, Howard, and Byrd (2010) showed that a structure like Hoag's Object can be formed in simulations by assuming a strong bar that gradually weakens. The strong bar makes sure that no other resonances survive except the Outer Lindblad Resonance. In their article they added an artificial potential for the bar to show that this hypothesis was possible.

In this study we will try to do something similar, but with a bar that forms itself from an initial model. Furthermore, our model will have a live dark matter halo and $\sim 10^7$ particles and is in three dimensions.

V. N-BODY SIMULATIONS

For our simulations we use a modified version of GalactICS (Widrow and Dubinski, 2005) to generate galaxy models. We use the Bonsai tree-code (Bédorf, Gaburov, and Portegies Zwart, 2012) for our simulation. In this section we explain our models, discuss our choice of parameters and finally discuss the N-Body code.

A. Model

We use a modified version of GalactICS, named galactics.parallel. It has been modified by Bédorf and Gaburov so it can be used by the Bonsai code. The parameters of our model can be found in Table II. We use an exponential disk, a Sérsic bulge, and a NFW dark halo. In Table III the mass, the outer radius and number of particles is given for each part of our model. In Fig. 4 we present the rotation curve of our model.

Our model is based on a model (md1mb1d1.5) described in Fujii, Bédorf, and Portegies Zwart (2016). The paper discusses the dynamics of stellar disks in live dark-matter halo's. We choose this model, because it developed the clearest ring structure after 10 Gyrs of simulation.

M_d ($10^{10}M_\odot$)	M_b ($10^{10}M_\odot$)	M_h ($10^{10}M_\odot$)	$R_{d,t}$ (kpc)	$R_{b,t}$ (kpc)	$R_{h,t}$ (kpc)	N_d	N_b	N_h
4.99	0.458	46.4	46.6	2.61	620	1.5M	0.14M	14.3M

TABLE III The mass, the outer radius and number of particles for the disk (d), bulge (b) and halo (h) from our model.

1. Halo

The NFW dark matter halo is based on the article from Navarro, Frenk, and White (1996). We will follow Widrow and Dubinski (2005) in describing the density profile and potential. The density profile is

$$\rho_{NFW}(r) = \frac{\rho_h}{(r/a_h)(1+r/a_h)^2}, \tag{5.1}$$

where a_h is the scale radius, $\rho_h \equiv \frac{\sigma_h^2}{4\pi a_h^2}$ is the characteristic density and σ_h is a characteristic velocity dispersion of the halo. The gravitational constant G is set equal to 1. We get the gravitational potential by solving the poison equation

$$\vec{\nabla}^2\Phi = 4\pi\rho \tag{5.2}$$

and require that the potential is equal to zero in infinity. We get

$$\Phi_{NFW}(r) = -\sigma_h^2 \frac{\log(1+r/a_h)}{r/a_h}. \tag{5.3}$$

If we leave it like this, the halo would be infinitely long and massive, which would be less than optimal for simulations. So there is a cutoff energy introduced $\mathrm{E}_h - \equiv \epsilon_h\sigma_h^2$, where ϵ_h is the cutoff parameter. For $\epsilon_h = 0$ it gives a full NFW profile. For $0 < \epsilon_h < 1$ it gives a truncated profile.

The model is further modified to give an option for rotation. This is the α parameter, which gives the fraction of particles that have positive angular momentum in the z-direction (J_z). And $1-\alpha$ gives the fraction of particles with negative J_z. Setting $\alpha = 0.5$ gives zero net rotation.

2. Disk

We assume an exponential disk, following Fujii, Bédorf, and Portegies Zwart (2016) we have a surface density distribution of

$$\Sigma(R) = \Sigma_0 \exp^{-R/R_d}. \tag{5.4}$$

The Σ_0 is the central surface density and R_d is the Disk scale length. Furthermore, the disk is truncated at radius R_{out}, with a sharpness defined by δR_{out}. Note that Σ_0 is not a parameter of the model, instead we use M_d which is the total disk mass. The structure of the disk in the z-direction is given by $\mathrm{sech}^2(z/z_d)$, where z_d is the disk scale height. The radial velocity dispersion is assumed to be $\sigma_R^2(R) = \sigma_{R0}^2 \exp^{-R/R_\sigma}$, where σ_{R0} is the radial velocity dispersion in the center of the disk and R_σ is the scale length for it. We assume that $R_\sigma = R_d$. For our disk we have Toomre's stability parameter Q (Binney and Tremaine, 2008) that is controlled by σ_{R0}. Our model is set up such that $Q = 1.2$ at a reference radius of $2.5R_d$.

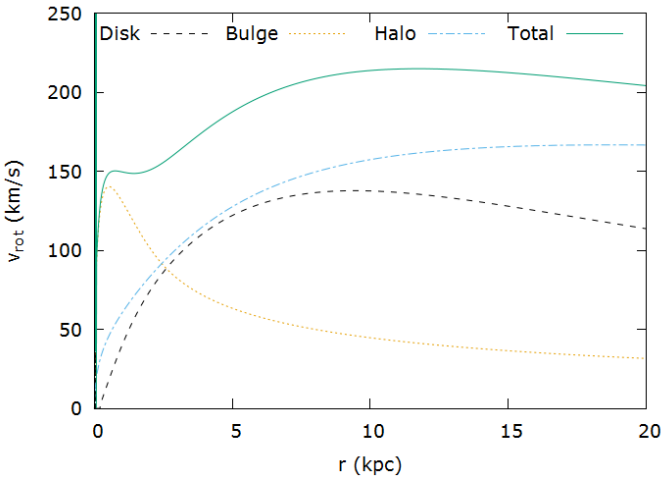

FIG. 4 This is the rotation curve of our model, obtained after generating the model.

3. Bulge

The Sérsic bulge is modeled after a Hernquist model (Hernquist, 1990). The density profile is given by

$$\rho_H = \frac{\rho_b}{(r/a_b)(1+r/a_b)^3} \tag{5.5}$$

and the potential is

$$\Phi_H = \frac{\sigma_b^2}{1+r/a_b}, \tag{5.6}$$

where we have the scale length a_b, the characteristic density $\rho_b = \sigma_b^2/(2\pi a_b^2)$ and the characteristic velocity σ_b. The model we use, is a truncated version of this Hernquist model. Just like the halo it has a truncation parameter ϵ_b. We assume no rotation of the bulge.

B. Code

As simulation code we use Bonsai developed by Bédorf, Gaburov, and Portegies Zwart (2012). This code is based on the tree method algorithm introduced by Barnes & Hut (Barnes and Hut, 1986). It scales as $O(n \log n)$, which makes it quicker than direct gravitational N-body algorithms that scale as $O(n^2)$. The special thing about this code is that it runs solely on the Graphics Processing Unit (GPU). The code is optimized for parallel clusters. This makes it possible to use over 10 million particles with even a modest computer like the Little Green Machine in Leiden.

For our simulations we use 16 million particles. Since we use a live halo, most of the particles are in this halo. The timestep we use is $dt = 0.305$ Myr. The softening is $\epsilon = 0.01$ kpc and the opening

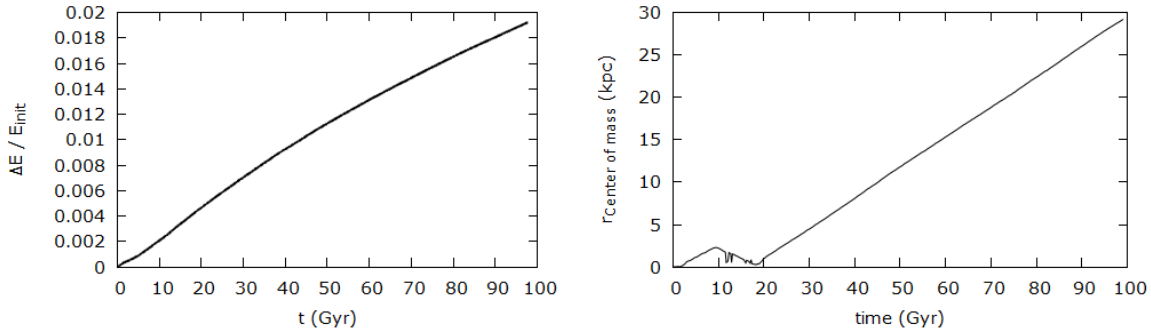

(a) Energy deviation

(b) Center of Mass deviation

FIG. 5 (a) Presented here is the fraction of the energy deviation with respect to the energy at the begin of the simulation. Energy is not conserved and is gained over the whole run. (b) Here is the radius of the center of mass plotted for the disk and bulge stars with respect to the center of mass at time zero.

angle for the tree-walk is $\theta = 0.4$. We rebuild the tree every timestep. We run our simulations for 97.7 Gyr, which is more then six times the Hubble Time. In other words we run the simulation for more than six times the age of Universe. The reason is that the initial conditions are artificial anyway. If we come across a result that looks like Hoag's Object even after Hubble Time, we could look back a few Gyr's and see if the conditions of the galaxy at that time are reasonable.

VI. RESULTS

In this section we present the results of our simulation. First we describe the procedure to get our results.

All our data is moved in such a way, that the center of mass of the bulge and disk stars is always at the origin. This is necessary as you can see in Fig. 5b, the center of mass doesn't stay in one place. It is a known problem that momenta is badly preserved in the tree-code (Hernquist, 1987).

In our simulations there appears a bar, thus we need a method to analyze the bar. We follow Fujii, Bédorf, and Portegies Zwart (2016) in our analyses of the bar. We use a Fourier decomposition of the surface density, we get

$$\frac{\Sigma(R,\varphi)}{\Sigma_0(R)} = \sum_{m=0}^{\infty} A_m(R)\cos m[\varphi - \varphi_m(R)], \tag{6.1}$$

here (R,φ) are polar coordinates, $\Sigma(R,\varphi)$ is the surface density at (R,φ), $\Sigma_0(R)$ is the surface density averaged over φ, and $A_m(R)$ and φ_m are the amplitude and phase angle of Fourier mode m. The m is what periodicity the density has, for a bar we have $m = 2$, since a bar makes two peaks in the surface density profile. Higher m is equivalent to spiral structure. How we got our Fourier constants from a Discrete Fourier Transform, can be found in Appendix A. A high A_m means that the m mode is strong. For our data we take radial bins of $\Delta r = 1$ kpc and angle bins of $\Delta\varphi = \frac{\pi}{180}$ radians. We define the bar strength as the maximum value of $A_2(R)$ for $R < 30$ kpc, we call the corresponding R, R_{max}. We define the angle of the bar as $\varphi_2(R_{max})$. We look from R_{max} forward

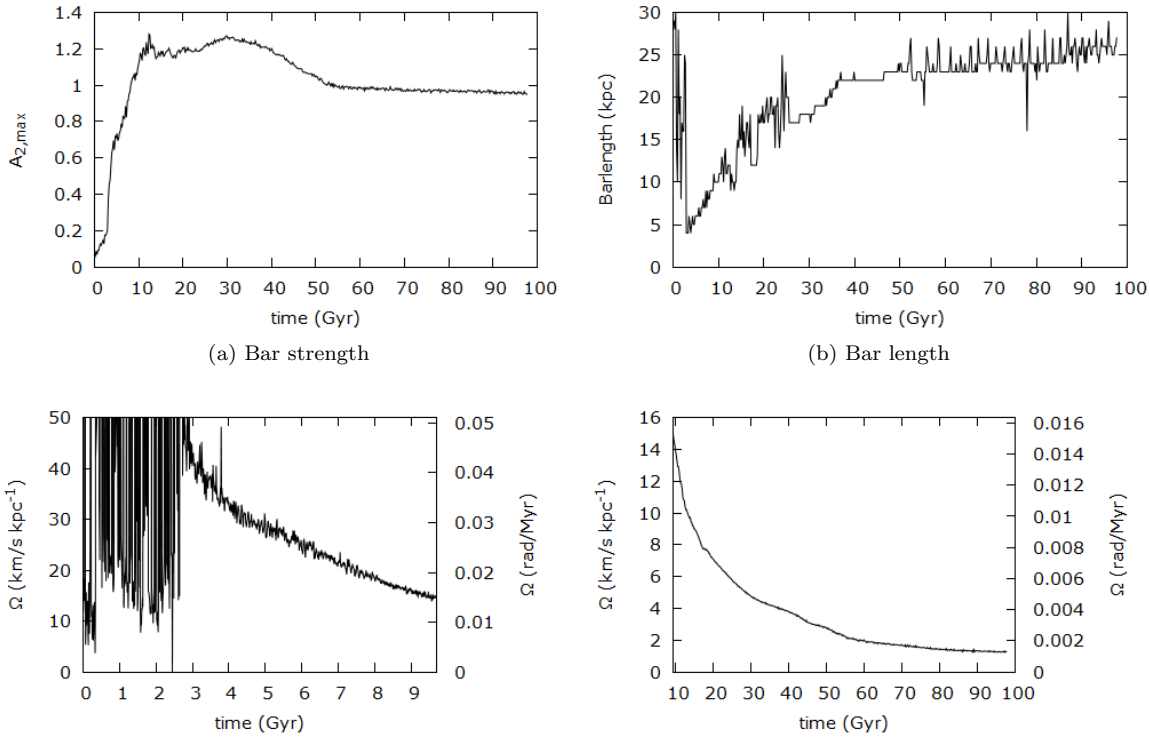

(a) Bar strength

(b) Bar length

(c) Bar speed

(d) Bar speed

FIG. 6 Here we present the properties of the bar from our simulation. In the upper left we have the maximal A_2 component for each time step, which is equivalent to the bar strength. In the upper right we plot the bar length. Lower left presents the bar speed up to 9.7 Gyr. In the lower right we have the bar speed from 9.5 Gyr and onward.

at $\varphi_2(R)$, the first R for which $|\varphi_2(R) - \varphi_2(R_{max})| > 0.05\pi$ radians is true we define as the end of the bar. This radius we take as the bar length. We do this every 1 time steps (≈ 0.02 Gyr) for the first 10 Gyr and every 20 time steps after that. From the angle of the bar, we can compute the pattern speed of the bar.

The data from the bar can be found in Fig. 6. If we look more closely at the plot of the bar strength (Fig. 6a), we see that A_2 grows from 0.1 to 1.3 in the first 12 Gyr, where it reaches it's maximum at 12 Gyr. It stays nearly flat (1.2 ± 0.1) from 12-30 Gyr, where it reaches a local maximum of 1.3 at 30 Gyr. After this it decreases steadily to a value of 1.0 at 55 Gyr. From this time onward it appears to be in a steady state, since the bar strength doesn't decrease more then 0.05 in a time frame of 42 Gyr. For this reason we wanted to have a snapshot from every stage of the bar. So we will compare snapshots from 0.00, 2.54, 11.7, 29.9, 54.3 and 97.7 Gyr.

In Fig. 7 you can see the density plots of the previous mentioned 6 snapshots. For the snapshots every bin has a size of 0.2 by 0.2 kpc. We look at our simulations from three sides, the top (xy-plane), the front (xz-plane) and the side (yz-plane). The density is displayed on a log scale, since this is similar as we would see in an observed galaxy.

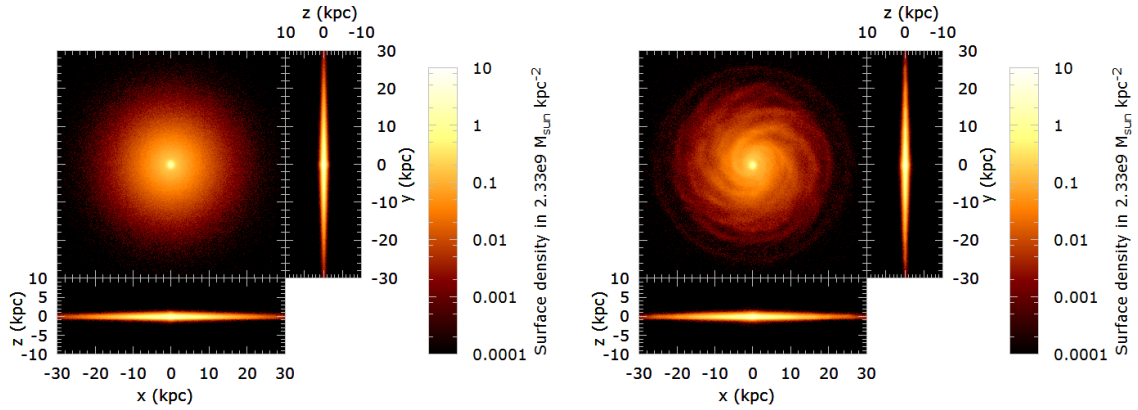

(a) 0.00 Myr

(b) 2.54 Myr

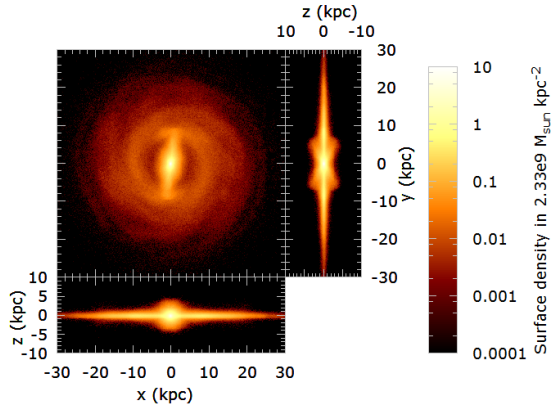

(c) 11.7 Gyr

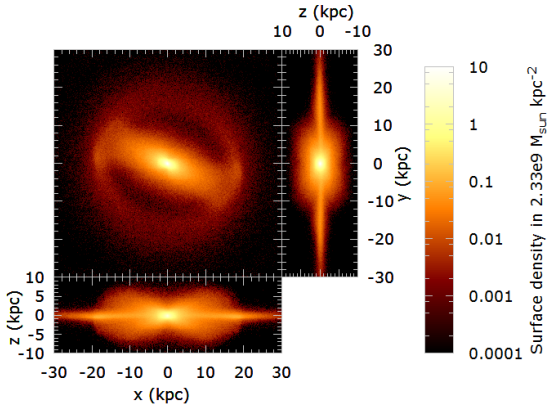

(d) 29.9 Gyr

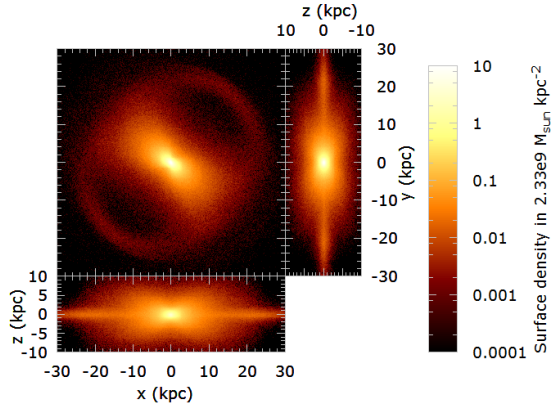

(e) 54.3 Gyr

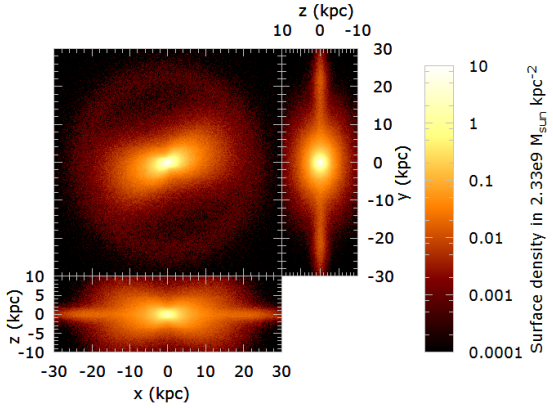

(f) 97.7 Gyr

FIG. 7 The surface density as seen from the top (xy-plane), front (xz-plane) and side (yz-plane) from our simulation. The positions of the stars have been modified such that the origin (0,0,0) coincides with the center of mass of the bulge and disk stars at that time. (a) is at the begin of our simulation and (f) is after the final time step.

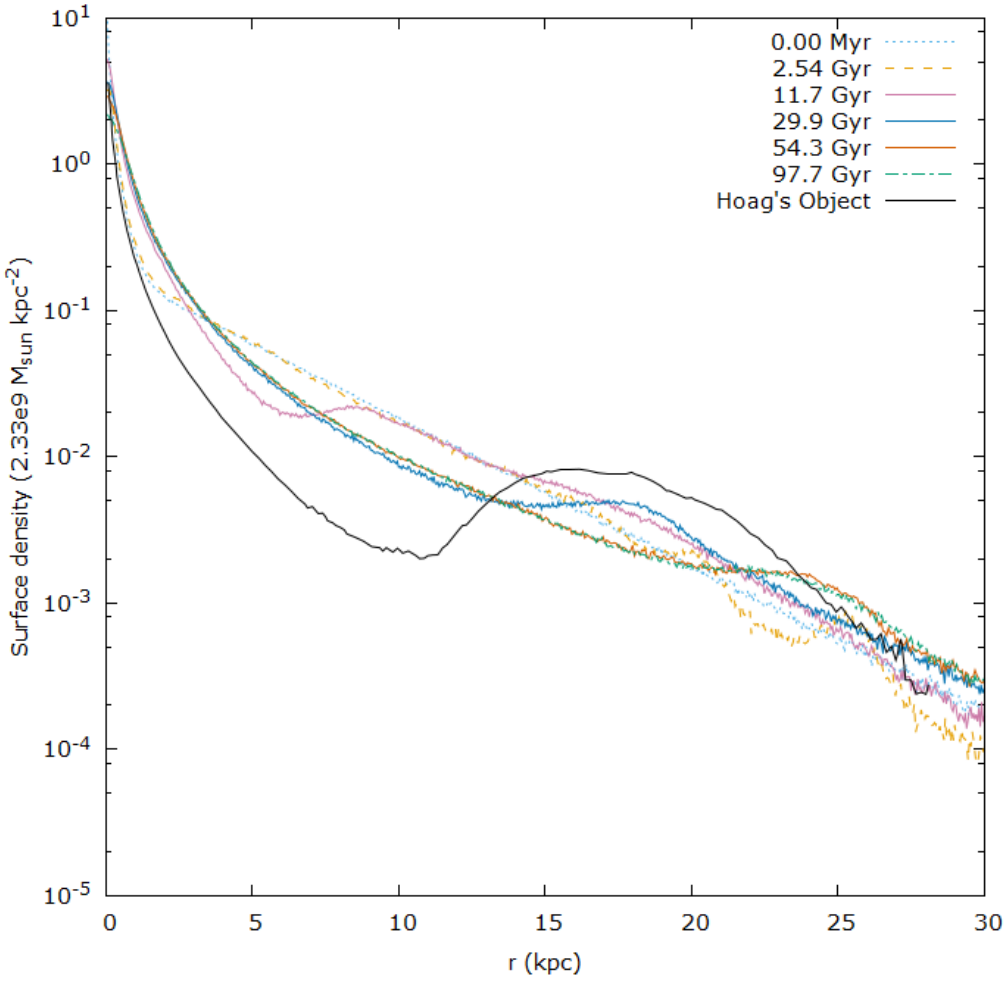

FIG. 8 The the average surface densities for each radius. We included the same data from Hoag's Object (see Fig. 3), where we scaled the central luminosity such that we could compare it with our simulation results.

The former mentioned plots are 2 dimensional, it's easier to compare the observations with a 1 dimensional plot. Thus we have Fig. 8. Here we look at the galaxy from the top, so we see the xy-plane. We averaged over the angle φ to get the surface density at a certain radius. We've also included the data from Fig. 3. We scaled the data from Hoag's Object such that the surface density of Hoag's Object is the same in $R = 0.085$ kpc as in the snapshot of 29.9 Gyr. Furthermore since magnitude and brightness are related through a $-2.5 \log_{10}$ relation, we've also applied this relation.

Lastly we have our Fig. 5 that tells us about the quality of our simulations. We measure the deviation of the total energy with respect to the initial energy. The fraction of this is what we plotted in Fig. 5a. In Fig 5b we present the deviation of the center of mass of the disk and bulge

stars.

VII. DISCUSSION

We discuss the quality of our simulation first. In Fig. 5a we see the error of the energy as fraction of the initial energy. The maximum energy error in one iteration is 1.34493×10^{-5} also as a fraction of the initial energy. This is comparable to the numerical precision. The energy error each time step is small en we see no sudden spikes. Hence nothing strange is happening during our simulation with respect to the energy. In Fig. 5b we see how the center of mass of the stars behaves. At first the center of mass moves away from the initial position, with a local maximum of 2.3 kpc at 9.3 Gyr. After that it nearly goes back to zero (0.2 kpc) at 20 Gyr, thereafter it grows linear up to a value of 29.1. Looking closer at the coordinates, it appears that z-coordinate is the main cause of this. First the z-coordinate becomes positive, until we see the peak at 9.3 Gyr. After that the z-coordinate decreases steadily up to a value of -29.0 kpc. The x,y coordinates are 0.14 kpc and 2.16 kpc at the last iteration. As the size of the galaxy is in the order of 30 kpc, we conclude that momentum is poorly preserved. Considering the density Fig.'s 7a - 7f, the figures still look like a normal galaxy. We don't see any strange patterns, so we suspect that this artifact doesn't influence the morphology of the galaxy. We therefore argue that this shifting of the galaxy don't influences our results and the simulation is satisfactory. If we would want to make our momentum conservation better, we would have to decrease our opening angle θ (Hernquist, 1987).

The main object of this research was to find out if we could form Hoag's Object from standard models of galaxies without other interactions. If we look at Fig.'s 7a - 7f we don't see a visual match. There is a ring visible in the last 4 snapshots, but this ring is not as broad as in Hoag's Object. The ring at 29.9 Gyr is the most similar. The main difference is that there is a bar present in these snapshots, but we see none in Hoag's Object. If we look at Fig. 8 we don't see a radial density profile that matches with Hoag's Object. For the snapshots from time 11.7 Gyr and onward we observe peaks in the density surface, just like the peak in Hoag's Object. The crests are at the same radius as the rings of Fig. 7, hence they represent the rings. These peaks are not as high as in Hoag's Object, except the one of 11.7 Gyr. In the ring the density is higher and its probably at the outer Lindblad resonance. These two factors should cause more star formation, thus younger stars. It has been shown that younger stars have a lower mass-to-light ratio (Charlot, Worthey, and Bressan, 1996), thus more light per unit mass. For example a 2 Gyr old stellar has a Mass-to-light ratio of $\sim 1.5 M_\odot/L_\odot$, while a 10 Gyr old star has a ratio of $\sim 5.4 M_\odot/L_\odot$. Therefore we argue that the crest of Hoag's Object luminosity profile should be lower. As we mentioned in section III.C the star population of the ring of Hoag's Object is 2 Gyr, while that of the core is 10 Gyr. Thus the ring appears 3.4 as massive in Fig. 8.

As mentioned before Freeman, Howard, and Byrd (2010) argued that the shape of Hoag's Object could be created by assuming a strong bar that disappears over a time. With our results we get a bar and a ring, but the bar doesn't seem to disappear. On the contrary the bar strength only seems to grow over time as we can see in Fig. 6a. Thus we haven't found something that resembles Hoag's Object.

Although we didn't find our desired result, let us analyze the results a bit more. We first look at the bar. The A_2 component reaches a value of 0.5 at 3.6 Gyr. From this time on we can say that there is a clear bar. This is also made clear in Fig.'s 6b and 6c, we see a well defined bar speed and bar length from time 3 Gyr and onward. Before this time, the values vary a lot and are not

continues. The bar reaches it's peak at 12 Gyr. The bar speed slows down exponentially, as seen in Fig. 6c and 6d. The bar length also grows in this period and becomes about twice as big.

The next interesting episode is from 12 Gyr to 30 Gyr. The strength profile is almost flat with values of A_2 between 1.1 and 1.3. The length keeps increasing from 10 kpc up to 18 kpc at 30 Gyr. The bar speed decreases exponentially, just like before. The peak in surface density as seen in Fig. 8 moves from 8.5 kpc to 17.7 kpc, this is the position of the ring. The ring is near the same position as the end of the bar, which is the bar length.

From 30 Gyr to 55 Gyr the bar strength decreases steadily to a value of $A_2 = 1.0$, but this value still correspond with a strong bar. The bar speed keeps decreasing exponentially. The bar length increases to 23 kpc. The peak in the radial surface density of Fig. 8 is at $20 \sim 24$ kpc. Thus the ring moves outward.

From 52 Gyr and onward the system seems to be at equilibrium. The A_2 value of the bar drops from 1.0 to 0.95, so it doesn't vary much. The bar length averages to a length of 25 kpc. The speeds keeps decreasing exponentially and the density profile from the snapshots at 54.3 and 97.7 Gyr are nearly indistinguishable in Fig. 8.

In the last 4 snapshots, Fig.'s 7c - 7f, we also see the boxy and peanut shape from the bar, if we look at it from the side. This is expected from a bar.

Athanassoula, Lambert, and Dehnen (2005) have shown that bars can be destroyed by a Central Mass Concentration (CMC). This Central Mass Concentration can be a combination of up to three things, a super massive black hole (that is observed in most disk galaxies), a molecular gas disk and/or a star bulge. This CMC has to be very large though, a fraction of $\frac{M_{CMC}}{M_{disk}} \approx 0.1$ is needed to completely destroy a bar and $\frac{M_{CMC}}{M_{disk}} \approx 0.01 \sim 0.05$ to weaken the bar. Here M_{CMC} is the mass of the CMC and M_{disk} is the mass of the disk. The extend of this CMC must also be small enough, $\frac{r_{cmc}}{r_{disk}} = 0.01 \sim 0.1$. It must be noted that this CMC is slowly introduced in the former mentioned paper, but not initially assumed. And we already have a bulge in our model, with a mass fraction that is $\frac{M_{bulge}}{M_{disk}} = 0.09$, and the typical range from the bulge divided by that of the disk is $\frac{a_{bulge}}{R_{disk}} = \frac{0.64}{4.2} = 0.15$ (see table II). Our halo mass on the other hand is quite large $\frac{M_{halo}}{M_{disk}} = 9.4$, but this fraction was equal to 5 in the paper of Athanassoula, Lambert, and Dehnen (2005). So to get a similar CMC we could increase the range of the disk, or decrease the range of the bulge. And we want to decrease the mass of the halo.

VIII. CONCLUSIONS

With our results we can conclude the following. Our results are not enough to disprove or prove that Hoag's Object was created by a weak-bar. With our initial conditions we didn't find a galaxy like Hoag's Object. The simulation does develop a clear ring, but also a bar. After a bar develops the bar strength increases and the bar doesn't disappear. The bar speed decreases exponentially and the position of the ring radius with time. For further study we would require a model with a less strong bar or a model where the bar disappears, but still creates a ring structure. To create such a galaxy within a Hubble time, the size of the disk should probably be increased. Now the ring was at 8.5 kpc at 11.7 Gyr, but in Hoag's Object the ring begins at 13.2 kpc. So a disk size that is 1.5 times bigger seems reasonable. If we keep the bulge the same size, we have a a bulge that could act as CMC that would weaken the bar, but for this to work we want to decrease the Halo mass by a factor of 2.

Furthermore simulations lasting more than 50 Gyrs might not give new results. For our model it

was at equilibrium after 50 Gyrs. It must be noted that this is only one simulation, further research could give a better answer to this.

ACKNOWLEDGMENTS

We thank Michiko Fujii for being a help with analyzing our data and being able to use a model she has was working on in our research.

REFERENCES

Amram, P., Mendes de Oliveira, C., Boulesteix, J., and Balkowski, C., A&A **330**, 881 (1998).
Athanassoula, E., Lambert, J. C., and Dehnen, W., MNRAS **363**, 496 (2005), astro-ph/0507566.
Barnes, J. and Hut, P., Nature **324**, 446 (1986).
Bédorf, J., Gaburov, E., Fujii, M. S., Nitadori, K., Ishiyama, T., and Portegies Zwart, S., in *Proceedings of the International Conference for High Performance Computing, Networking, Storage and Analysis, p. 54-65* (2014) pp. 54–65, arXiv:1412.0659.
Bédorf, J., Gaburov, E., and Portegies Zwart, S., Journal of Computational Physics **231**, 2825 (2012), arXiv:1106.1900 [astro-ph.IM].
Binney, J. and Tremaine, S., *Galactic Dynamics: Second Edition, by James Binney and Scott Tremaine. ISBN 978-0-691-13026-2 (HB). Published by Princeton University Press, Princeton, NJ USA, 2008.* (Princeton University Press, 2008).
Brosch, N., A&A **153**, 199 (1985).
Brosch, N., Finkelman, I., Oosterloo, T., Jozsa, G., and Moiseev, A., MNRAS **435**, 475 (2013), arXiv:1307.6368.
Buta, R., ApJS **96**, 39 (1995).
Byrd, G. G., Freeman, T., and Buta, R. J., AJ **131**, 1377 (2006).
Charlot, S., Worthey, G., and Bressan, A., ApJ **457**, 625 (1996).
Finkelman, I., Moiseev, A., Brosch, N., and Katkov, I., MNRAS **418**, 1834 (2011), arXiv:1108.3079.
Freeman, T., Howard, S., and Byrd, G. G., Celestial Mechanics and Dynamical Astronomy **108**, 23 (2010).
Fujii, M. S., Bédorf, J., and Portegies Zwart, S., "The dynamics of stellar disks in live dark-matter halo," (2016), article in preperation.
Hernquist, L., ApJS **64**, 715 (1987).
Hernquist, L., ApJ **356**, 359 (1990).
Hoag, A. A., AJ **55**, 170 (1950).
Navarro, J. F., Frenk, C. S., and White, S. D. M., ApJ **462**, 563 (1996), astro-ph/9508025.
Schweizer, F., Ford, Jr., W. K., Jedrzejewski, R., and Giovanelli, R., ApJ **320**, 454 (1987).
Widrow, L. M. and Dubinski, J., ApJ **631**, 838 (2005), astro-ph/0506177.

Appendix A: Discrete Fourier Transform

Following Fujii, Bédorf, and Portegies Zwart (2016), we want to do the following Fourier transformation

$$\frac{\Sigma(R,\phi)}{\Sigma_0(R)} = \sum_{m=0}^{\infty} A_m(R)\cos m[\phi - \phi_m(R)], \tag{A1}$$

But from our data we can only make a Discrete Fourier Transform. We look at the case that n is even, for n is odd the result is the same, except for $\frac{n+1}{2}$, but we are not interested in $\frac{n+1}{2}$ for now. At a certain R, this gives

$$\frac{\Sigma(\phi)}{\Sigma_0} = \sum_{m=-n/2}^{n/2} B_m e^{\phi i m}, \tag{A2}$$

where B_m is a complex number, $B_m = |B_m|e^{i\mathrm{Arg}(B_m)}$ and $B_{-m} = B_m^*$ is the complex conjugate of B_m since our input is real. We look at the case that n is even, for n is odd the result is the same, except for $\frac{n+1}{2}$, but we are not interested in $\frac{n+1}{2}$ right now. Thus we get

$$\sum_{m=-n/2}^{n/2} B_m e^{\phi i m} = \sum_{m=0}^{n/2} (B_m e^{\phi i m} + B_{-m} e^{-\phi i m}) \tag{A3a}$$

$$= \sum_{m=0}^{n/2} (|B_m| e^{i\mathrm{Arg}(B_m)} e^{\phi i m} + |B_{-m}| e^{i\mathrm{Arg}(B_{-m})} e^{-\phi i m}) \tag{A3b}$$

$$= \sum_{m=0}^{n/2} (|B_m| e^{i\mathrm{Arg}(B_m)} e^{\phi i m} + |B_m| e^{-i\mathrm{Arg}(B_m)} e^{-\phi i m}). \tag{A3c}$$

Because $|B_{-m}| = |B_m|$ and $\mathrm{Arg}(B_{-m}) = -\mathrm{Arg}(B_m)$.

(A3d)

$$= \sum_{m=0}^{n/2} (|B_m| e^{i(\mathrm{Arg}(B_m)+\phi m)} + |B_m| e^{-i(\mathrm{Arg}(B_m)+\phi m)}). \tag{A3e}$$

Here we see the sum of two numbers that are conjugated to each other, then this relation holds $z + z^* = a + bi + a - bi = 2a$. So

$$= \sum_{m=0}^{n/2} 2\ \mathrm{Re}(|B_m| e^{i(\mathrm{Arg}(B_m)+\phi m)}) \tag{A3f}$$

$$= \sum_{m=0}^{n/2} 2|B_m| \cos(\phi m + \mathrm{Arg}(B_m)). \tag{A3g}$$

And we can conclude that $A_m = 2|B_m|$ and $\phi_m = -\frac{\mathrm{Arg}(B_m)}{m}$